Design Methodology for Aeroelastic Tailoring of Additively-Manufactured Lattice Structures using Low-Order Methods

Max M. J. Opgenoord*
Massachusetts Institute of Technology, Cambridge, Massachusetts 02139

Karen E. Willcox†
University of Texas at Austin, Austin, Texas 78712

Additively-manufactured wings can be aeroelastically tailored, which offers potential for increased air vehicle efficiency via lighter structures. This paper develops a methodology to design aeroelastically-tailored wings using additively-manufactured lattice structures. Adaptive meshing techniques are used to design the topology of the lattice to align with the load direction and the lattice is optimized to minimize the structural weight and to improve the flutter margin. To alleviate the computational effort of aeroelastically tailoring a structure, a low-order model for the dynamics of the lattice structure is developed. This structural low-order model is coupled to a previously-developed physics-based transonic flutter model to compute the aeroelastic behavior of wings with internal lattice structures. The structural low-order model is validated by comparing against the full-order structural dynamics model. Finally, the design methodology is applied to the design of an internal structure of an aircraft wing to increase that wing's flutter speed.

Nomenclature

AR	=	Aspect ratio
A_Γ, $A_{\dot{\Gamma}}$, A_κ	=	Coefficients of Γ evolution equation
a_{ik}	=	Cross-sectional area of member connecting node i and k
c	=	Airfoil chord length
E	=	Young's modulus
$\mathbf{F}$	=	Force vector
h	=	Vertical deflection, positive downward
$\boldsymbol{\mathcal{I}}_{\bar{y}}$	=	Mass moment of inertia per span
$\boldsymbol{K}$	=	Stiffness matrix
L	=	Lift per span
$\bar{l}$	=	Effective wing length
l_{ik}	=	Length of strut connecting node i and k
$\boldsymbol{M}$	=	Mass matrix
$\boldsymbol{\mathcal{M}}$	=	Mass per span
M_∞	=	Freestream Mach number
$M_{c/2}$	=	Aerodynamic moment per span around mid-chord
m	=	Number of members in lattice
m_{wing}	=	Wing mass
n	=	Number of nodes in lattice
$\boldsymbol{\mathcal{S}}_{\bar{y}}$	=	Mass unbalance per span
$\boldsymbol{T}_{()\to()}$	=	Map between low-order and full-order lattice model
t	=	Time
q_∞	=	Dynamic pressure

*Former Postdoctoral Research Associate, Department of Aeronautics and Astronautics; mopg@mit.edu. Member AIAA.
†Director, Institute of Computational Engineering and Sciences; kwillcox@ices.utexas.edu. Fellow AIAA.

$\mathbf{u}$	=	Displacement vector
$V_\perp$	=	Wing-perpendicular velocity
V_f	=	Flutter speed
w	=	Vertical (downward) velocity
$\bar{x}, \bar{y}, \bar{z}$	=	Coordinates aligned with swept wing
Γ	=	Circulation strength
θ	=	Pitch angle
κ_x	=	x-doublet strength
Λ	=	Wing sweep angle
λ	=	Taper ratio
σ	=	Stress
σ_T	=	Maximum tensile stress
σ_C	=	Maximum compressive stress
φ	=	Basis function (normalized)
$\chi_{\mathfrak{fl}}$	=	Maximum real eigenvalue of aeroelastic system

I. Introduction

The additional design freedom that is offered by additive manufacturing can be potentially be used to efficiently alter the aeroelastic properties of wings to improve their flutter margins. In this paper we develop a design methodology to exploit this additional design freedom to aeroelastically tailor the internal structure of aircraft wings.

To date, the aeroelastic optimization of aircraft wings has mostly focused on conventional internal wing structures—i.e., an orthogonal array of ribs and spars [1–5]. Novel manufacturing techniques potentially allow for further improvements in the structural efficiency of wings with configurations that are not necessarily restricted to a conventional rib-spar lay-out. Several ways to parametrize the internal structure of the wing have been demonstrated. For example, Balabanov and Haftka [6], and Locatelli et al. [7] retained the rib-spar layout but allowed for curvilinear components, which is therefore an inherently two-dimensional parametrization. Alternatively, three-dimensional parametrizations are used where the optimizer is allowed to place material anywhere in the wing. These problems are typically solved using solid-isotropic-material-with-penalization (SIMP) methods [8–10] or level-set methods [11, 12], as demonstrated by, amongst others, Maute and Reich [13], Dunning et al. [14], and Kambampati et al. [15] for aircraft wings and wing boxes. A combination of a conventional wing structure layout with topologically optimized parts is investigated by Stanford and Dunning [16] where an orthogonal rib-spar layout is used but where topology optimization is applied to the ribs and spars. Recently, Townsend et al. [17] optimized plate-like wing structures using level-set topology optimization to minimize the weight of the wing and to mitigate flutter, and demonstrated large weight savings by using such an optimized structure. Finally, Aage et al. [18] used topology optimization to design the internal structure of an aircraft wing using giga-voxel resolution, but that study did not consider aerostructural coupling or dynamic aeroelasticity.

Other studies have shown the potential benefits of novel manufacturing techniques on a wing's aeroelastic properties. For example, Haddadpour et al. [19] and Stodieck et al. [20] demonstrated increased wing stiffness for tow-steering with composite materials [21, 22]. Stanford et al. [23] investigated the differences between several novel tailoring schemes on wings subject to transonic flutter constraints and found that a spatially varying thickness distribution—through additive manufacturing—yielded more benefit than tow-steering alone.

Lattice structures have been used in the design of internal wing structures by Walker et al. [24], who optimized the internal structure of a wing using lattice structures utilizing commercial software, focusing on lattice structures due to their high stiffness-to-weight ratio [25]. Such lattice structures have also been used in morphing wing applications [26, 27]. Neither of these studies considered aeroelasticity, whereas the focus of the current paper is on design of lattice structures for wings under aeroelasticity constraints.

Beyond aircraft wings, helicopter and propeller blades have also been aeroelastically optimized. For example, Ganguli et al. [28] used high-fidelity flow and structural simulations to minimize rotor vibrations, while constraining aeroelastic stability. Glaz et al. [29] also focused on minimizing vibrations in helicopter forward flight, now using surrogate models for the structural and aerodynamic loads. Finally, Pagano et al. [30] instead focused on noise reduction of propeller blades through coupled aeroelastic-aeroacoustic simulations.

Our methodology instead focuses on the aeroelastic tailoring of additively-manufactured lattice structures for wings. To reduce the computational effort required for this—and thereby enabling inclusion in early-stage design methods—we develop a lower-order method for the structural dynamics of lattice structures, which we then combine

with a previously-developed aerodynamic low-order model to assess the aeroelastic behavior of a lifting surface. This design methodology is applicable to (UAV) wings, for which an example is included.

The low-order models used to design the lattice and describe its aeroelastic behavior are discussed in Section II. The structural response found by the low-order structural model is validated for different beams in Section III. The design methodology is applied to a wing design study in Section IV. Finally, the main findings are discussed in Section V.

II. Methodology

This section details the aeroelastic tailoring approach, which is developed in this paper and summarized in Section II.A. Throughout this work, we use a previously-developed physics-based low-order aerodynamic model (Section II.B) which is then coupled to a newly-developed low-order structural dynamics model of the lattice (Section II.C) to describe the aeroelastic response of the structure. The structure is aeroelastically-tailored by altering the cross-sectional area of the struts in the lattice (Section II.D).

II.A. Aeroelastic Tailoring Approach

The complete aeroelastic tailoring approach can be summarized as follows. This work uses a previously-developed physics-based low-order model for transonic flutter [31, 32]. The first step, therefore, is to calibrate the aerodynamic coefficients of that model using 2D unsteady Euler simulations for the airfoil family used in the wing design. This approach is described in detail in Ref. [31, 32].

Second, the load distribution over the wing is computed to obtain the baseline lift coefficient c_{ℓ_0} at each beam section—which is needed to select the correct aerodynamic coefficients for the flutter model [32]—and to generate a pressure field over the wing that is subsequently used as input to the structural analysis of the wing internal structure. There are several ways of computing the flow over the wing, e.g., using a vortex-lattice method or a higher-fidelity Euler simulation. In the current work, we use an Euler CFD simulation computed with the SU2 tool suite [33].

The aerodynamic loading of the wing is used as input to design a lattice structure for the internal wing structure. Lattice design results in a high-dimensional optimization problem to decide on the size of the struts, nodal locations and connectivity between nodes. To address the high dimensionality of the problem, the design of a lattice structure is split into the design of the lattice topology—the location of the lattice nodes and the connectivity between those nodes—and the sizing of the lattice struts. Combining both these optimization problems, however, can potentially lead to more efficient solutions, and this is a topic of future work, as described in Ref. [34].

The pressure distribution over the wing is used as the input for the structural FEM analysis of the internals of the wing, which allows for computing the stress tensor everywhere in the domain. The stress tensor is computed using a finite element method for linear elasticity.* From the stress tensor, then, a Riemannian metric field is computed to define where the lattice should be fine (near areas of high stress) and where it can be coarse (near areas of low stress). That metric is used to generate a lattice topology that is optimal using a metric-based adaptive mesh generator. A similar approach is used in the CFD community to adapt meshes to detailed flow features [36]. Once the topology is decided on, the struts of that lattice can be optimized for minimum weight. Here, we use bar elements for the struts with pinned joints—in future work a higher-fidelity (and more expensive) approach would be to use 3-D beam elements in combination with modeling the joint stiffnesses. Currently, we also do not account for material overlap near the joint. Note that the low-order dynamics model for the structure also would work with such a higher-fidelity underlying full-order model. In this work, the strut sizes are minimized for weight, subject to a flutter constraint. Note that the struts are considered cylinders here, but the approach extends to other cross-sectional shapes as well.

The overall design methodology is illustrated in Fig. 1 and described in detail in Ref. [34]. An example of a bracket designed using this design methodology is shown in Fig. 2.†

Finally, the size of each strut of this lattice is determined by solving an optimization problem that takes into account compatibility conditions, buckling, and flutter. To determine whether or not flutter occurs for such a lattice structure, we build up a low-order structural model for the lattice and combine that with the low-order aerodynamic model.

*This solver is described in detail in Appendix B of Ref. [35] and its source code is made available at github.com/mopg/luteos.jl.

†The geometry generation method that was used to generate the solid geometry in Fig. 2b is described in detail in Appendix C of Ref. [35] and its source code is made available at github.com/mopg/intrico.jl.

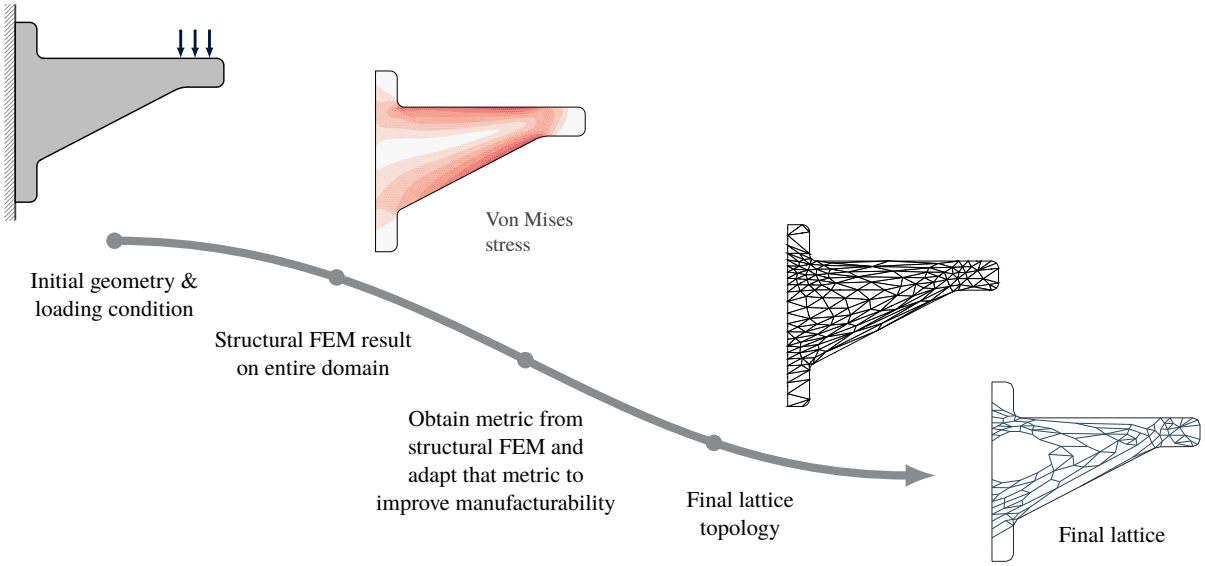

Fig. 1 Approach for design of lattice structures for additive manufacturing [34].

II.B. Low-Order Aerodynamic Model

We tailor the internal lattice structure of the wing such that the wing has minimum weight while mitigating flutter, potentially at transonic flow conditions. At transonic Mach numbers, Theodorsen theory with compressibility corrections is no longer accurate. Instead, we employ a physics-based low-order model for transonic flutter [31, 32]. This section briefly summarizes the physics-based model's formulation; for more details, see Ref. [31] and [32].

This low-order flutter model is calibrated using 2D unsteady high-fidelity Euler simulations and validated against standard flutter benchmark cases, where it is shown to accurately capture the characteristic transonic dip behavior. The model's application to the flutter characteristics of wings is described in Ref. [32].

The aerodynamic model uses strip theory, which is applicable to wings with moderate-to-high aspect ratio. For instance, at the ith section on the wing, the evolution equation for the circulation perturbation $\Delta\Gamma_i$ can be written as [32]

$$\begin{aligned}\Delta\dot{\Gamma}_i = &-\frac{A_\Gamma}{A_{\dot{\Gamma}}}\Delta\Gamma_i - \frac{A_\kappa}{A_{\dot{\Gamma}}}\Delta\kappa_{x,i} + \frac{1}{A_{\dot{\Gamma}}}\left(\Delta w_i + V_\perp \frac{\partial \Delta h_i}{\partial \bar{y}_i}\tan\Lambda\right)\\ &+ \frac{V_\perp}{A_{\dot{\Gamma}}}\Delta\theta_i + \frac{c_i/4}{A_{\dot{\Gamma}}}\left(\Delta\omega_i + V_\perp \frac{\partial \Delta\theta_i}{\partial \bar{y}_i}\tan\Lambda\right),\end{aligned} \tag{1}$$

where h is the (downward) deflection, w is the vertical (downward) velocity, θ is the pitch angle, ω is the angular velocity, c is the local chord, Λ is the wing sweep angle, and $V_\perp$ is the wing-perpendicular velocity. κ_x is the doublet strength, which is the second aerodynamic state per section. Note that the subscript $()_i$ indicates the section number. The aerodynamic coefficients A_Γ, $A_{\dot{\Gamma}}$, A_κ are all calibrated from unsteady 2D transonic Euler simulations, as described in Ref. [31].

The circulation strength perturbation $\Delta\Gamma_i$ and its time derivative $\Delta\dot{\Gamma}_i$ are then used to compute the circulatory parts of the lift perturbation and the moment perturbation. These are combined with the non-circulatory parts (which are functions of $\Delta\dot{\theta}$, $\Delta\ddot{\theta}$ and $\Delta\ddot{h}$) to give the lift perturbation ΔL_i and moment perturbation $\Delta M_{c/2}$. For more information, please refer to Refs [31, 32].

In Ref. [32], the flutter model is coupled to a one-dimensional Euler-Bernoulli beam model. Here, we replace that beam model with a low-order lattice model, which is further described in Section II.C.

II.C. Low-Order Structural Dynamics Model for Lattice Structures

To compute the dynamic characteristics of lattice structures for the internal structure of a wing efficiently, we develop a low-order model for the lattice structure dynamics. This dynamic low-order model is defined in terms of the vertical and angular displacement of the wing sections (Fig. 3), which are needed for the aerodynamic model. The

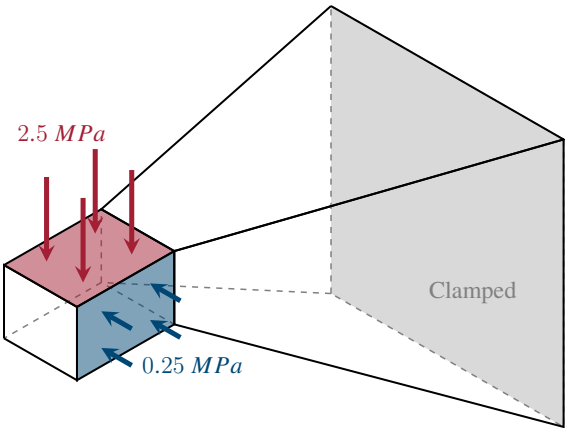

(a) Load case. The bracket is loaded in bending and clamped at the back.

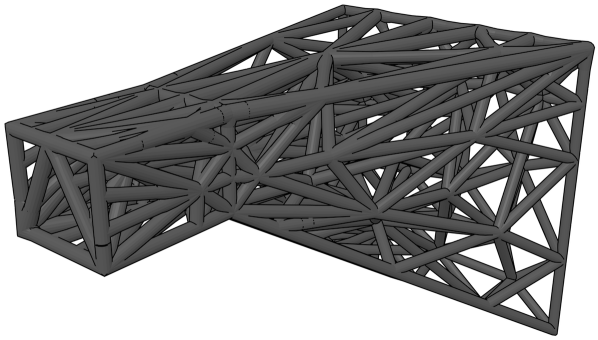

(b) Final design. The lattice is fine near areas of high stress and aligned with the load direction.

Fig. 2 Example of a bracket designed using the lattice design methodology. Figure from Ref. [34].

purpose of this low-order model is therefore two-fold: (1) to change the structural system's degrees of freedom into degrees of freedom that are relevant for the aerodynamic mode, and (2) reduce the cost of computing eigenvalues of the aeroelastic system by keeping the number of DOFs for the structural system around the same order of magnitude as for the aerodynamic system. Note that in order to achieve (1) we have to map between low-order and full-order model, and those mappings are then used to construct a lower-order model to reduce the computational effort (2).

For a lattice structure with n nodes and m struts, the dynamics are described by

$$\boldsymbol{M}\ddot{\mathbf{u}}\,(t) + \boldsymbol{K}\mathbf{u}\,(t) = \mathbf{F}\,(t), \tag{2}$$

where $\boldsymbol{M} \in \mathbb{R}^{3n\times 3n}$ is the mass matrix, $\boldsymbol{K} \in \mathbb{R}^{3n\times 3n}$ is the stiffness matrix, $\mathbf{F}\,(t) \in \mathbb{R}^{3n}$ is a dynamic force vector, and $\mathbf{u}\,(t) \in \mathbb{R}^{3n}$ is the displacement vector of each node in the lattice.

$\boldsymbol{K}$ and $\boldsymbol{M}$ are potentially large (sparse) matrices, resulting in a large aeroelastic system. As part of the lattice optimization, the eigenvalues of this aeroelastic system need to be computed repeatedly, which can become expensive. Therefore, we reduce the size of the structural system by using an equivalent beam model (Fig. 3), which describes the vertical and torsional deflection of several wing sections, rather than the deflection of each lattice node. The dynamics of the beam model are described by,

$$\begin{bmatrix} \boldsymbol{\mathcal{M}} & \boldsymbol{\mathcal{S}}_{\bar{y}} \\ \boldsymbol{\mathcal{S}}_{\bar{y}} & \boldsymbol{\mathcal{I}}_{\bar{y}} \end{bmatrix} \begin{bmatrix} \ddot{\mathbf{h}} \\ \ddot{\boldsymbol{\theta}} \end{bmatrix} + \begin{bmatrix} \boldsymbol{K}_{hh} & \boldsymbol{K}_{h\theta} \\ \boldsymbol{K}_{\theta h} & \boldsymbol{K}_{\theta\theta} \end{bmatrix} \begin{bmatrix} \mathbf{h} \\ \boldsymbol{\theta} \end{bmatrix} = \begin{bmatrix} -\mathbf{L} \\ \mathbf{M}_{c/2} \end{bmatrix}, \tag{3}$$

where $\mathbf{h}$ are the vertical deflections of the wing sections and $\boldsymbol{\theta}$ are the torsional deflections of the wing sections. $\mathbf{L}$ is the lift acting at each wing section, and $\mathbf{M}_{c/2}$ is the moment around the mid-chord at each wing section. The matrices $\boldsymbol{\mathcal{M}}$, $\boldsymbol{\mathcal{S}}_{\bar{y}}$, and $\boldsymbol{\mathcal{I}}_{\bar{y}}$ are computed from the full-order mass matrix $\boldsymbol{M}$, and the matrices $\boldsymbol{K}_{hh}$, $\boldsymbol{K}_{h\theta}$, $\boldsymbol{K}_{\theta h}$, and $\boldsymbol{K}_{\theta\theta}$ are computed from the full-order stiffness matrix $\boldsymbol{K}$. The expressions for these low-order matrices are derived in the rest of this section. Note that this low-order model approach is agnostic to how the full-order structural dynamics are modeled. The approach therefore remains the same irrespective of whether bar or beam elements are used for the lattice struts—even though the eventual low-order system is obviously different. This approach can also be extended to consider more than just twisting and bending, by defining appropriate mappings to other directions. However, we focus here on bending and twisting as those are most important for aeroelasticity.

The full-order mass matrix $\boldsymbol{M}$ is obtained by lumping half the weight of each strut connecting to a node into the mass of that node, while having massless connectors (Fig. 4).

We define the low-order mass matrix $\boldsymbol{\mathcal{M}}$ as a diagonal matrix, where the ith diagonal entry corresponds to the mass per span of the ith beam section. Similarly, $\boldsymbol{\mathcal{S}}_{\bar{y}}$ is a diagonal matrix where the diagonal represents the mass unbalance per span at each beam section. Finally, $\boldsymbol{\mathcal{I}}_{\bar{y}}$ is a diagonal matrix of the mass moment of inertia per span at each beam section.

The low-order mass matrix $\boldsymbol{\mathcal{M}}$ (diagonal by construction) is mapped from the full-order mass matrix $\boldsymbol{M}$ as

$$\operatorname{diag}(\boldsymbol{\mathcal{M}}) = \boldsymbol{T}_{\boldsymbol{M}\to\boldsymbol{\mathcal{M}}} \operatorname{diag}(\boldsymbol{M}), \tag{4}$$

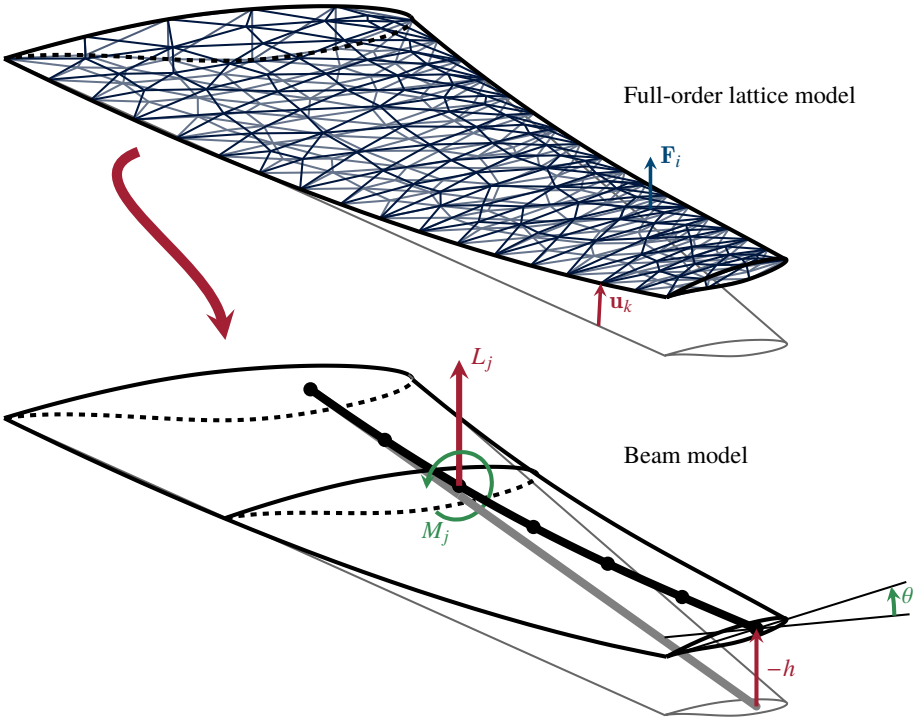

Fig. 3 The full-order dynamic lattice model is reduced to a low-order lattice model to be used in the lattice optimization.

where $\boldsymbol{T}_{\boldsymbol{M}\to\boldsymbol{\mathcal{M}}}$ is defined as

$$T_{M_k\to\mathcal{M}_j} = \varphi_j(\bar{y}_k), \tag{5}$$

with φ_j the basis function of the jth node and $\bar{y}$ the coordinate along the elastic axis of the wing. Throughout this work, linear nodal basis functions are used for φ_j. Note that all basis functions are normalized, i.e., $\int_0^{\bar{l}} \varphi_j(\bar{y})\mathrm{d}\bar{y} = 1$. By using linear basis functions ("hat functions"), we lump half of the mass between beam sections into the equivalent mass of the adjacent beam sections. The resulting mass matrix is sometimes referred to as a *diagonally lumped mass matrix* [37], All quantities necessary for the mapping between the beam model and the full-order model are defined in Fig. 5.

The mass unbalance matrix $\boldsymbol{\mathcal{S}}$ is found in a similar fashion as the low-order mass matrix. However, for the mass unbalance, we also care about the local perpendicular distance to the elastic axis of the node, because the effect of the center of gravity of a section is encoded in the mass unbalance matrix. Hence, we obtain $\boldsymbol{\mathcal{S}}$ (again, diagonal by construction) from a similar mapping from the mass matrix $\boldsymbol{M}$ as,

$$\mathrm{diag}\left(\boldsymbol{\mathcal{S}}_{\bar{y}}\right) = \boldsymbol{T}_{\boldsymbol{M}\to\boldsymbol{\mathcal{S}}}\,\mathrm{diag}\left(\boldsymbol{M}\right) \tag{6}$$

with

$$T_{M_k\to\mathcal{S}_j} = \varphi_j(\bar{y}_k)\left(\bar{x}_k - \bar{x}_j\right). \tag{7}$$

Again, $\varphi_j(\bar{y}_k)$ proportionally lumps the local nodal contribution into the adjacent beam sections, while $\left(\bar{x}_k - \bar{x}_j\right)$ is the perpendicular distance to the elastic axis.

Finally, the mass matrix $\boldsymbol{M}$ maps to the mass moment of inertia matrix $\boldsymbol{\mathcal{I}}_{\bar{y}}$ as

$$\mathrm{diag}\left(\boldsymbol{\mathcal{I}}_{\bar{y}}\right) = \boldsymbol{T}_{\boldsymbol{M}\to\boldsymbol{\mathcal{I}}}\,\mathrm{diag}\left(\boldsymbol{M}\right) \tag{8}$$

with

$$T_{M_k\to\mathcal{I}_j} = \varphi_j(\bar{y}_k)\left[\left(\bar{x}_k - \bar{x}_j\right)^2 + \left(\bar{z}_k - \bar{z}_j\right)^2\right]. \tag{9}$$

Here, the last term indicates the square of the perpendicular distance to the elastic axis, because the sectional moment of inertia needs to be computed around the elastic axis, not the local nodal axis. Note that we are hereby neglecting the inertia of the node itself, which is a higher-order effect.

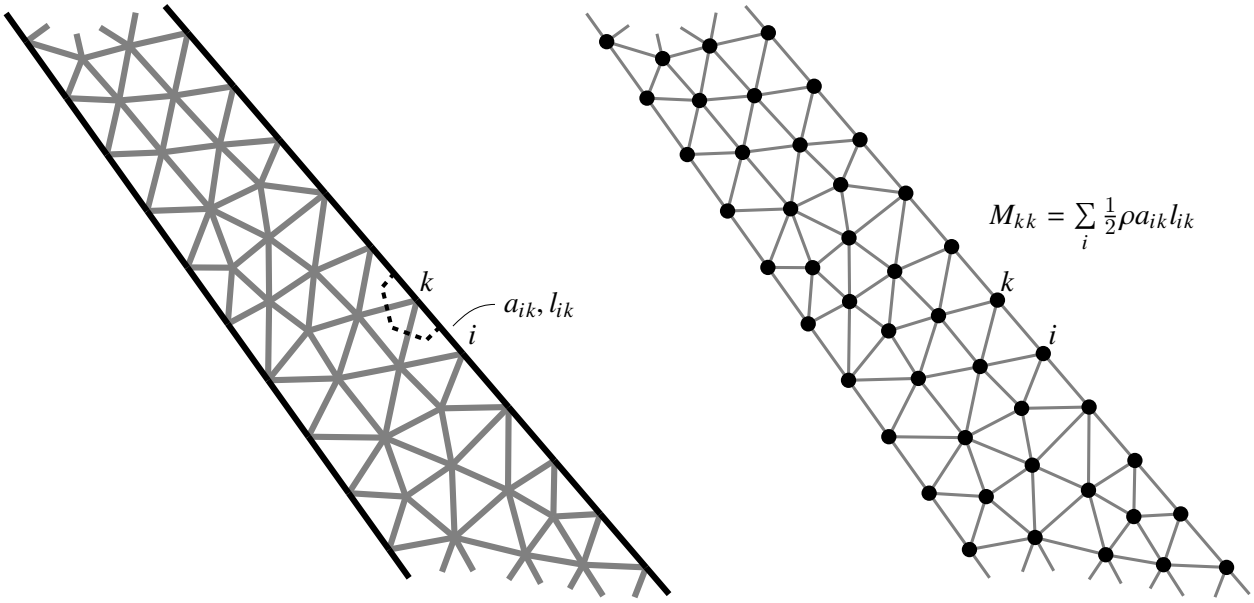

Fig. 4 Mass matrix is generated by lumping the mass from the edges into the nodes.

To fully define the beam model (3), we also need to compute the low-order stiffness matrices. The stiffness matrix $\boldsymbol{K}$ is obtained from the connectivity of the lattice ($\boldsymbol{C}$) and stress-strain relations ($\boldsymbol{B}$) as [38]

$$\boldsymbol{K} = \boldsymbol{C}\boldsymbol{B}^{-1}\boldsymbol{C}^{\mathsf{T}}. \tag{10}$$

For this beam model, we only consider bending around the $\bar{x}$ axis and torsion around the $\bar{y}$ axis. Therefore, we only have to consider displacements in z-direction. To find the stiffness matrices for the beam model, we consider the combined full-order system ($\boldsymbol{K}\mathbf{u} = \mathbf{f}$) with the low-order model's degrees of freedom ($\mathbf{h}$ and $\boldsymbol{\theta}$),

$$\begin{bmatrix} \boldsymbol{K} & \mathbf{0} & \mathbf{0} \\ \boldsymbol{T}_{\mathbf{u}\to\mathbf{h}} & -I & \mathbf{0} \\ \boldsymbol{T}_{\mathbf{u}\to\boldsymbol{\theta}} & \mathbf{0} & -I \end{bmatrix} \begin{bmatrix} \mathbf{u} \\ \mathbf{h} \\ \boldsymbol{\theta} \end{bmatrix} = \begin{bmatrix} \boldsymbol{T}_{\mathbf{L}\to\mathbf{F}} \\ \mathbf{0} \\ \mathbf{0} \end{bmatrix} \mathbf{L} + \begin{bmatrix} \boldsymbol{T}_{\mathbf{M}\to\mathbf{F}} \\ \mathbf{0} \\ \mathbf{0} \end{bmatrix} \mathbf{M}_{c/2}, \tag{11}$$

where $\boldsymbol{T}_{\mathbf{u}\to\mathbf{h}}$, $\boldsymbol{T}_{\mathbf{u}\to\boldsymbol{\theta}}$, $\boldsymbol{T}_{\mathbf{L}\to\mathbf{F}}$, and $\boldsymbol{T}_{\mathbf{M}\to\mathbf{F}}$ are mappings between the low-order and full-order model, which will be defined later in this section. As written, Eq. (11) simply holds the full-order static displacement relations $\boldsymbol{K}\mathbf{u} = \mathbf{f}$, where $\mathbf{f}$ is mapped from from the lower-order aerodynamic lift and moment, and holds the relations that $\boldsymbol{T}_{\mathbf{u}\to\mathbf{h}}\mathbf{u} = \mathbf{h}$ and $\boldsymbol{T}_{\mathbf{u}\to\mathbf{h}}\boldsymbol{\theta} = \boldsymbol{\theta}$. Through Schur complements of Eq. (11), this system can be rewritten as

$$\begin{bmatrix} \boldsymbol{T}_{\mathbf{u}\to\mathbf{h}}\boldsymbol{K}^{-1}\boldsymbol{T}_{\mathbf{L}\to\mathbf{F}} & \boldsymbol{T}_{\mathbf{u}\to\mathbf{h}}\boldsymbol{K}^{-1}\boldsymbol{T}_{\mathbf{M}\to\mathbf{F}} \\ \boldsymbol{T}_{\mathbf{u}\to\boldsymbol{\theta}}\boldsymbol{K}^{-1}\boldsymbol{T}_{\mathbf{L}\to\mathbf{F}} & \boldsymbol{T}_{\mathbf{u}\to\boldsymbol{\theta}}\boldsymbol{K}^{-1}\boldsymbol{T}_{\mathbf{M}\to\mathbf{F}} \end{bmatrix} \begin{bmatrix} \mathbf{L} \\ \mathbf{M}_{c/2} \end{bmatrix} = \begin{bmatrix} \mathbf{h} \\ \boldsymbol{\theta} \end{bmatrix}, \tag{12}$$

which combines Eq. (2) with mappings between the full displacement vector $\mathbf{u}$ and the vertical displacement (positive downward) h and the angular displacement θ, as well as mappings between the full force vector $\mathbf{F}$ and the lift vector $\mathbf{L}$ and the moment around the mid-chord $\mathbf{M}_{c/2}$. To find the low-order stiffness matrices, the block inverse of Eq. (12) is computed, yielding the system

$$\begin{bmatrix} \boldsymbol{K}_{hh} & \boldsymbol{K}_{h\theta} \\ \boldsymbol{K}_{\theta h} & \boldsymbol{K}_{\theta\theta} \end{bmatrix} \begin{bmatrix} \mathbf{h} \\ \boldsymbol{\theta} \end{bmatrix} = \begin{bmatrix} -\mathbf{L} \\ \mathbf{M}_{c/2} \end{bmatrix} \tag{13}$$

To map the full displacement vector $\mathbf{u}$ to the deflection of the beam model $\mathbf{h}$, we consider the average z-displacement near the beam node,

$$T_{u_{z,k}\to h_j} = \frac{\mathcal{A}_k \varphi_j(\bar{y}_k)}{\sum_i \mathcal{A}_i \varphi_j(\bar{y}_i)}, \tag{14}$$

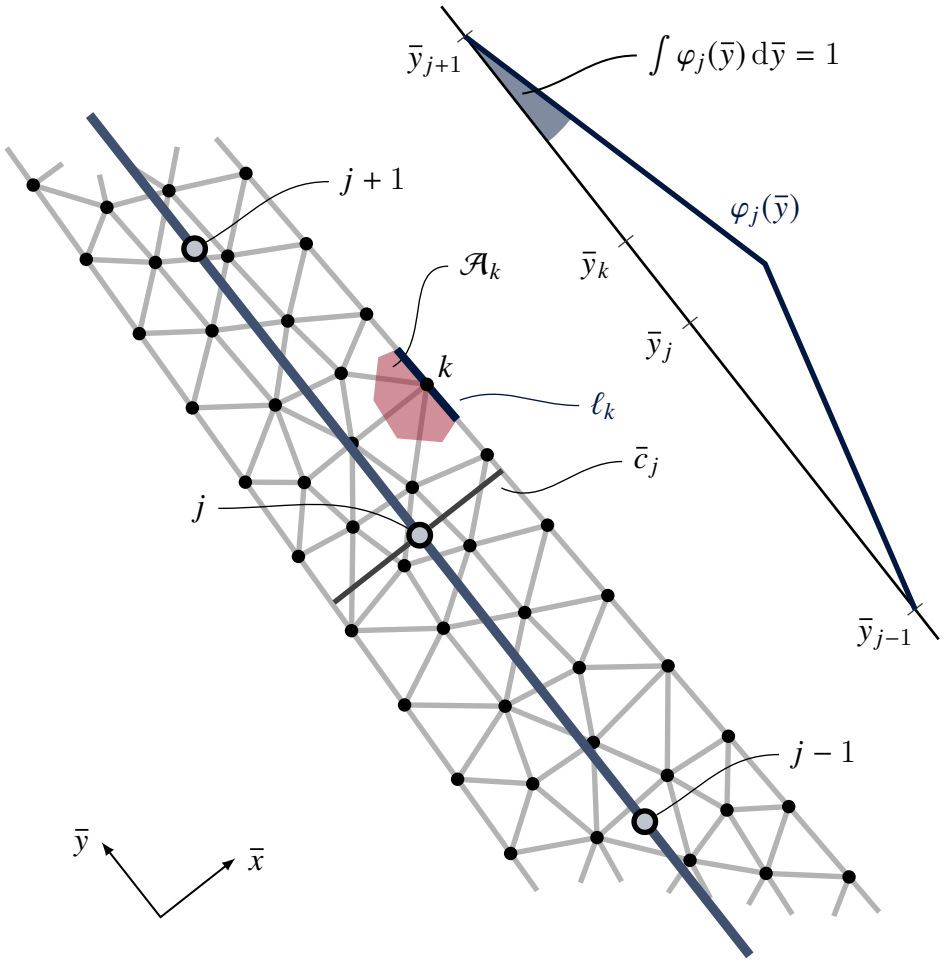

Fig. 5 Mapping the deflections from the low-order beam model to the full lattice model.

where $\mathcal{A}_k$ is the projected area in z-direction of the kth lattice node (Fig. 5). The full displacement vector $\mathbf{u}$ can also induce a pitch deflection of the beam model; the mapping between $\mathbf{u}$ and $\boldsymbol{\theta}$ is defined to be

$$T_{u_{z,k}\to\theta_j} = \frac{1}{2}\frac{\ell_k\varphi_j(\bar{y}_k)}{\sum_i \ell_i\varphi_j(\bar{y}_i)}\frac{1}{\bar{x}_k - \bar{x}_j}, \tag{15}$$

where ℓ_k is the length along the leading or trailing edge for the lattice node k.

The lift per span $\mathbf{L}$ only acts on the surface of the lattice, and is mapped to the full force vector $\mathbf{F}$ by considering the average pressure around the jth beam node,

$$T_{L_j\to F_{k,z}} = \frac{1}{\bar{c}_j}\varphi_j(\bar{y}_k)\mathcal{A}_k,$$

where $\bar{c}_j$ is the wing-perpendicular chord length at the jth wing section, and $\mathcal{A}_k$ is the projected area of the kth node, as defined in Fig. 5.

Finally, the moment around mid-chord per span $\mathbf{M}_{c/2}$ is mapped to the full force vector $\mathbf{F}$ as,

$$T_{M_j\to F_{k,z}} = \ell_k\,\varphi_j(\bar{y}_k)\,\frac{1}{\bar{x}_k - \bar{x}_j}. \tag{16}$$

The mappings $T_{u_{z,k}\to h_j}$, $T_{u_{z,k}\to\theta_j}$, $T_{L_j\to F_{k,z}}$, and $T_{M_j\to F_{k,z}}$ fully define the low-order structural model (3). That beam model has four states per beam section: the vertical (downward) deflection h_i, the vertical (downward) velocity w_i, the pitch angle θ_i and the pitch rate ω_i. Combined with the aerodynamic states ($\Delta\Gamma$, $\Delta\kappa_x$, $\Delta\dot{\kappa}_x$), the aeroelastic system therefore has seven states per beam section.

II.D. Lattice Optimization with Flutter Constraint

To find the optimal area of each strut in the lattice, we solve a nonlinear optimization problem, which includes limits on the stresses in each strut, buckling constraints, and constraints on flutter behavior. This optimization problem for a lattice with m struts and n nodes in the physical dimension d is written as

$$
\begin{aligned}
\min_{\mathbf{u},\mathbf{a},\mathbf{f},\boldsymbol{\sigma}} \quad & \mathcal{V} = \mathbf{l}^\mathsf{T}\mathbf{a} && \\
\text{subject to} \quad & \boldsymbol{C}\mathbf{f} = \mathbf{F} && \text{(force balance)} \\
& \boldsymbol{B}\boldsymbol{\sigma} + \boldsymbol{C}^\mathsf{T}\mathbf{u} = \mathbf{0} && \text{(stress-strain compatibility)} \\
& f_j = \sigma_j a_j && \text{(stress definition)} \\
& -\sigma_C \leq \sigma_j \leq \sigma_T && \text{(stress limits)} \\
& f_j \geq -\frac{\pi E a_j^2}{4(k_e l_j)^2} && \text{(buckling)} \\
& \chi_{\text{fl}} < \chi_{\text{fl,max}} && \text{(flutter)} \\
& a_{\min,j} \leq a_j \leq a_{\max,j} && \\
& \mathbf{u} \in \mathbb{R}^{n\,d},\ \mathbf{f} \in \mathbb{R}^m, &&
\end{aligned}
\tag{17}
$$

where $\mathcal{V}$ is the volume of the lattice, a_j is the cross-sectional area of the jth lattice strut, f_j is the force in the jth lattice strut, σ_j is the stress in the jth lattice strut, and l_j is the length of the jth strut. k_e is the column effective length factor, which is taken to be 1.2 here, σ_T is the maximum allowable tensile stress, and σ_C is the maximum allowable compressive stress. χ_{fl} is the maximum real part of the eigenvalues of the aeroelastic system, which is constrained to be lower than $\chi_{\text{fl,max}}$ (typically $-0.005/s$) for aeroelastic stability, similar to the work of Ringertz [39]. Note that apart from the flutter constraint, the optimization problem in Eq. (17) is used commonly in structural optimization problems [38].

χ_{fl} is computed using the low-order structural dynamic model (explained in Section II.C) to reduce the computational cost of the optimization problem in Eq. (17). However, the full-order structural model is still used to compute stresses and strains and enforce the stress and strain constraints throughout the part. These constraints are highly localized and it is therefore harder to come up with a global low-order model for those.

The optimization problem in Eq. (17) is non-convex, due to the constraint $f_j = \sigma_j a_j$ and the flutter constraint being non-convex. The problem is therefore solved using a generic NLP solver, in this case Ipopt [40]. Due to the non-convex nature of the problem, we cannot guarantee finding a global minimum. Therefore, the optimization problem can be solved with multiple initial conditions to find (a possibly lower) local minimum. But again, there is no guarantee that the global minimum can be found, even with multiple starts.

Since we are solving Eq. (17) using a generic nonlinear optimizer, providing gradients of the objective and constraints can greatly improve the speed and accuracy of the optimization. For the objective function, computing the gradient is straightforward as the objective function is linear. All constraints—except the flutter constraint—are also all linear or at most quadratic, for which it is straightforward to derive the gradients. However, the flutter constraint is a highly nonlinear function of the cross-sectional area of each strut.

Computing the gradient through finite differences or forward differentiation is too expensive for the flutter constraint, as gradient computation using such forward methods scales with the input dimension, and there can be thousands of struts in the wing lattice. Adjoint differentiation on the other hand, scales with the output dimension. Here, we are only interested in one output: the aeroelastic eigenvalue. We therefore implement an adjoint to efficiently compute the gradient of the maximum eigenvalue with respect to the cross-sectional areas of the struts. We derive the adjoint for this problem from adjoints of elementary matrix operations, based on the work by Giles [41, 42].

To compute the adjoint of χ_{fl}, the low-order model construction has to be traversed in reverse. Starting with the eigenvalue computation, the adjoint of a generic matrix $\boldsymbol{A}$ with respect to its maximum eigenvalue is

$$
\overline{\boldsymbol{A}} = \boldsymbol{R}^{-\mathsf{T}}\overline{\boldsymbol{\Lambda}}\boldsymbol{R}^\mathsf{T}, \tag{18}
$$

where the adjoint is here denoted as $\overline{\boldsymbol{A}}$, $\boldsymbol{R}$ is the matrix composed of eigenvectors and

$$
\overline{\boldsymbol{\Lambda}} = \begin{bmatrix} 1 & 0 & \cdots & 0 \\ 0 & 0 & \cdots & 0 \\ \vdots & \vdots & \ddots & \vdots \\ 0 & 0 & \cdots & 0 \end{bmatrix}, \tag{19}
$$

if the eigenvalues are ordered such that the first eigenvalue of $\boldsymbol{A}$ has the largest positive real part. Using this elementary result—more details are provided in Ref. [35]—we can compute the adjoint of the low-order mass and stiffness matrices in Eq. (3).

The part of the adjoint of the cross-sectional areas that stems from the mass matrix $\boldsymbol{M}$ follows in a straightforward manner from the adjoint of the low-order mass matrices and the mapping between the low-order mass matrix and the full mass matrix. For the stiffness matrices, we require the adjoint of a block inverse to compute the adjoints of the blocks in Eq. (12). This derivation is too long to repeat here, please consult Ref. [35] for more details.

We would then like to compute the adjoint of $\boldsymbol{K}$ using the adjoint of a matrix triple inverse product ($\boldsymbol{D} = \boldsymbol{C}\boldsymbol{A}^{-1}\boldsymbol{B}$), which is derived in Ref. [35]. In the following, we denote the different blocks of Eq. (12) as $\boldsymbol{K}_{11} = \boldsymbol{T}_{\mathbf{u}\to\mathbf{h}}\boldsymbol{K}^{-1}\boldsymbol{T}_{\mathbf{L}\to\mathbf{F}}$, $\boldsymbol{K}_{12} = \boldsymbol{T}_{\mathbf{u}\to\mathbf{h}}\boldsymbol{K}^{-1}\boldsymbol{T}_{\mathbf{M}\to\mathbf{F}}$, etc. The adjoint of the stiffness matrix $\boldsymbol{K}$ can then be expressed as

$$\frac{\partial \chi}{\partial \boldsymbol{K}} = -\left(\boldsymbol{K}^{-\mathsf{T}}\boldsymbol{T}_{\mathbf{u}\to\mathbf{h}}^{\mathsf{T}}\right)\frac{\partial \chi}{\partial \boldsymbol{K}_{11}}\left(\boldsymbol{K}^{-1}\boldsymbol{T}_{\mathbf{L}\to\mathbf{F}}\right)^{\mathsf{T}} \tag{20}$$

$$-\left(\boldsymbol{K}^{-\mathsf{T}}\boldsymbol{T}_{\mathbf{u}\to\mathbf{h}}^{\mathsf{T}}\right)\frac{\partial \chi}{\partial \boldsymbol{K}_{12}}\left(\boldsymbol{K}^{-1}\boldsymbol{T}_{\mathbf{M}\to\mathbf{F}}\right)^{\mathsf{T}} \tag{21}$$

$$-\left(\boldsymbol{K}^{-\mathsf{T}}\boldsymbol{T}_{\mathbf{u}\to\boldsymbol{\theta}}^{\mathsf{T}}\right)\frac{\partial \chi}{\partial \boldsymbol{K}_{21}}\left(\boldsymbol{K}^{-1}\boldsymbol{T}_{\mathbf{L}\to\mathbf{F}}\right)^{\mathsf{T}} \tag{22}$$

$$-\left(\boldsymbol{K}^{-\mathsf{T}}\boldsymbol{T}_{\mathbf{u}\to\boldsymbol{\theta}}^{\mathsf{T}}\right)\frac{\partial \chi}{\partial \boldsymbol{K}_{22}}\left(\boldsymbol{K}^{-1}\boldsymbol{T}_{\mathbf{M}\to\mathbf{F}}\right)^{\mathsf{T}}. \tag{23}$$

Note that here $\boldsymbol{K}^{-1}$ is always grouped with a projection matrix to avoid having to directly compute the inverse of $\boldsymbol{K}$ (a large sparse matrix). The part of the adjoint of the cross-sectional areas that stems from the stiffness matrix $\boldsymbol{K}$ then follows from the adjoint of $\boldsymbol{B}^{-1}$ in a straightforward manner as each diagonal entry of $\boldsymbol{B}^{-1}$ is linearly dependent on the cross-sectional area of one strut.

The contributions of the mass and stiffness matrix to the adjoint of the cross-sectional areas of the struts are added to yield the gradient of the maximum eigenvalue with respect to the cross-sectional areas of the lattice struts.

In our implementation, computing the adjoint is only 3.5× more expensive than evaluating the maximum aeroelastic eigenvalue, starting from low-order model construction. Computing a gradient of a function should be no more than five times as expensive as evaluating the underlying function [43], so this implementation is well within that.

III. Validation of Low-Order Structural Beam Model

The low-order beam model has to be validated against its full-order lattice model. We compare the frequencies and mode shapes for a long and slender beam, as computed by the full-order lattice model and the low-order beam model. A symmetric lattice that is used in the first part of this section is shown Fig. 6. This lattice is symmetric with respect to the yz plane with the elastic axis and center of gravity coinciding with the mid-chord line. The lattice's dimensions are $1.0 \times 20.0 \times 0.15$ m, the struts have a radius of 25 mm, and its material's Young's modulus is 70 GPa.

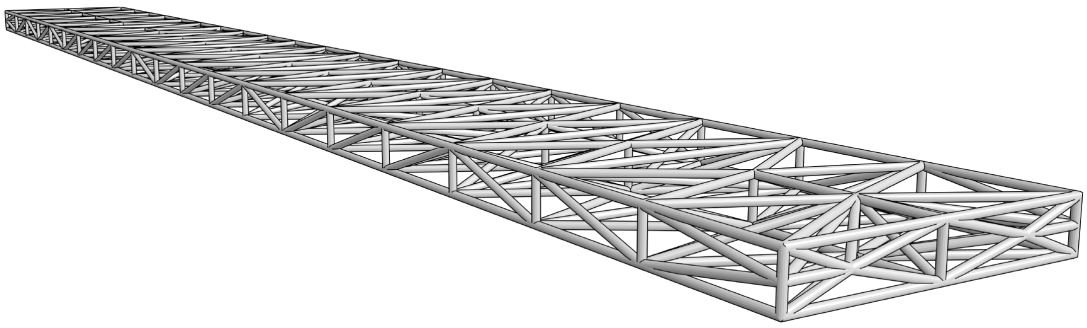

Fig. 6 Lattice with 136 nodes and 535 struts used for validation.

The frequencies of the model are listed in Table 1 for the first four bending modes and first two torsion modes using a beam model with $n_{\text{red}} = 10$ and $n_{\text{red}} = 20$ beam sections. The error between low-order and full-order model is below

4% in all cases, which is deemed sufficiently accurate in this study, as the error is lower than the spacing of frequencies between different modes. Note that the error increases for higher mode numbers, which is the result of the discretization in the beam model. As the number of beam sections in the beam model increases, the error frequencies and mode shapes further reduces (Table 1).

Mode	Lattice model, *Hz*	Beam model, *Hz*		Error, %		L^2 error in mode shape	
		$n_{\text{red}} = 10$	$n_{\text{red}} = 20$	$n_{\text{red}} = 10$	$n_{\text{red}} = 20$	$n_{\text{red}} = 10$	$n_{\text{red}} = 20$
Bending (I)	0.9075	0.9055	0.9061	0.22	0.15	0.003	0.0006
Bending (II)	5.263	5.306	5.286	0.81	0.44	0.011	0.005
Torsion (I)	9.152	9.111	9.16	0.45	0.087	0.007	0.004
Bending (III)	14.24	14.52	14.35	1.9	0.74	0.021	0.008
Bending (IV)	26.73	27.82	27.13	3.9	1.5	0.037	0.014
Torsion (II)	28.38	28.42	28.41	0.14	0.11	0.022	0.0115

Table 1 Comparison between frequencies obtained from the full-order lattice model and the low-order beam model.

Note that other model reduction approaches, such as a modal structural approximation, would capture lower modes exactly. Modal analysis has long been used in structural dynamics in various settings, such as in component substructuring [44]. However, in order to compute that approximation, we would have to solve a (potentially large) eigenvalue problem, which we try to avoid. Furthermore, in our approach, we reduce the model to degrees of freedom we care about for the aerodynamic model. Because we have to do these mappings from the full-order structural model to the aerodynamic model anyway, we also use these mappings to define a more efficient lower-order structural model.

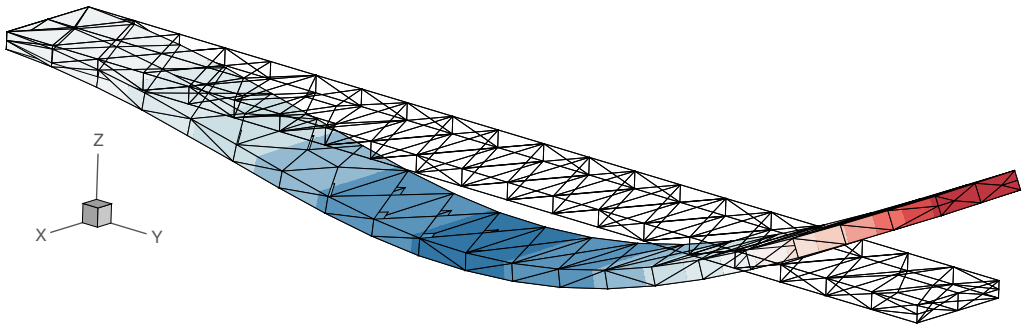

(a) Full-order lattice model

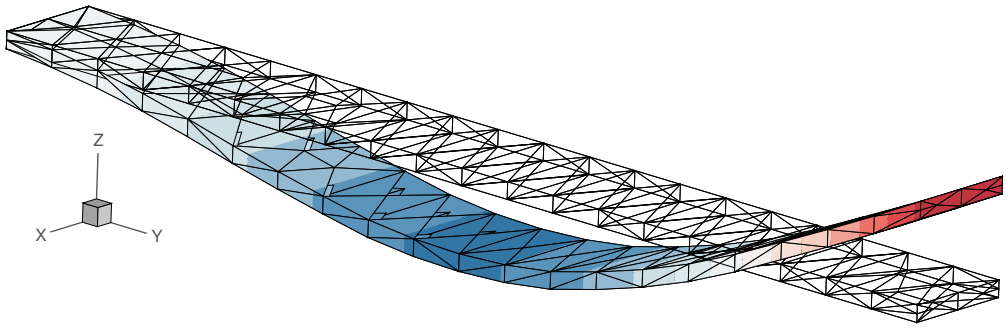

(b) Low-order beam model

Fig. 7 Comparison between second bending mode of full-order lattice model and low-order beam model. Note that the color scale is the same between figures.

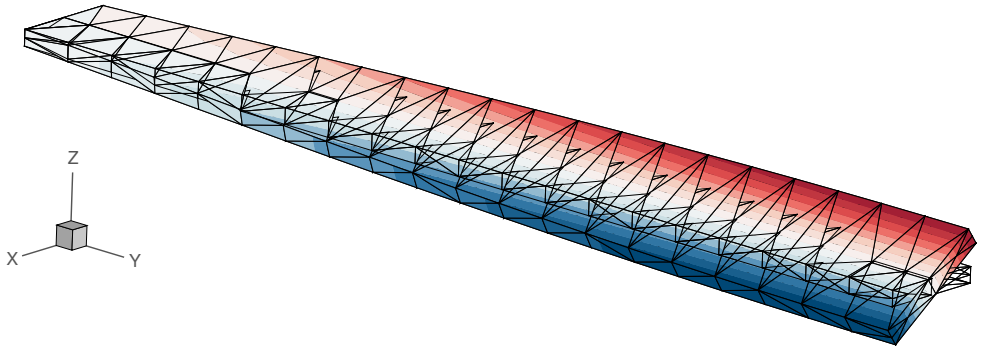

(a) Full-order lattice model

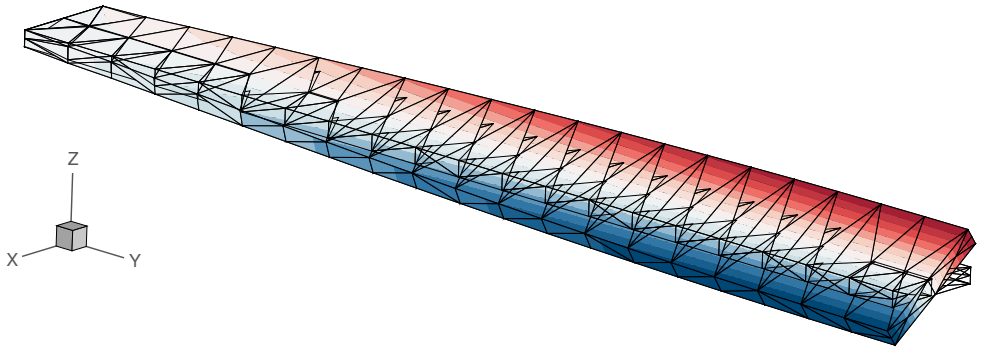

(b) Low-order beam model

Fig. 8 Comparison between first torsion mode of full-order lattice model and low-order beam model. Note that the color scale is the same between figures.

The mode shapes are also compared between the low-order beam model and full-order lattice model; visually in Figures 7 and 8 and quantitatively through the L^2 error in mode shape in Table 1. The second bending mode shape is shown in Fig. 7. These shapes also match well between the low-order model and full-order model. A comparison between the low-order model and full-order model for the first torsion mode is shown in Fig. 8, and again these shapes match well between the low-order and full-order model.

Lastly, we also compare the structural frequencies between the low-order and full-order model for a lattice where neither the elastic axis, nor the center of gravity position coincides with the mid-chord line. This lattice has an asymmetric orientation for its struts as well as different thicknesses for several struts (Fig. 9). The lattice's dimensions are again $1.0 \times 20.0 \times 0.15$ m and the material's Young's modulus is still 70 GPa. The radius of the struts in the center of the lattice is 5 mm (white in Fig. 9). The radius of the struts on the positive-x face are 3.5 mm (blue in Fig. 9), whereas the struts on the negative-x face are 7.1 mm (red in Fig. 9), to make the structure asymmetric.

Mode	Lattice model, Hz	Beam model, Hz	Error, %
Mode I	1.103	1.112	0.81
Mode II	6.620	6.398	3.5
Mode III	9.716	9.433	3.0
Mode IV	17.59	16.94	3.7
Mode V	31.59	30.17	4.4
Mode VI	33.03	31.67	4.1

Table 2 Comparison between frequencies obtained from the full-order lattice model and the low-order beam model for a case where the center of gravity and elastic axis do not coincide with the mid-chord.

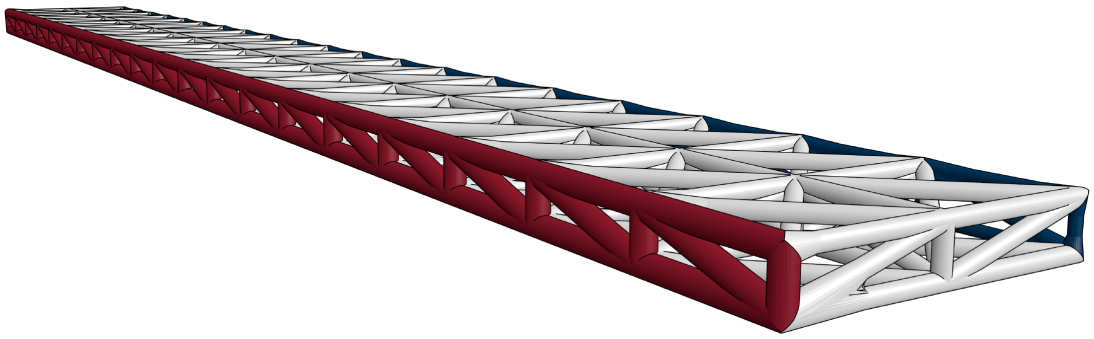

Fig. 9 Asymmetric lattice with 126 nodes and 489 struts used for validation of lattice structures. The cross-sectional area of the red struts is twice as large as that of the white struts, which in turn is twice the size of the cross-sectional area of the blue struts.

The structural frequencies for the lattice in Fig. 9 obtained from both the low-order model (10 beam sections) and full-order model are compared in Table 2. The error in frequency is comparable to the symmetric case (Table 1).

IV. Flutter Mitigation through Aeroelastic Tailoring

This section demonstrates the aeroelastic tailoring of lattice structures to mitigate flutter. First, we optimize the internal lattice of the wing without considering flutter and show the flutter boundary and structural modes of that design. Second, we optimize the internal lattice again, but now including a flutter constraint in the optimization. We then compare the flutter characteristics of the two wings as well as their relative mass. It is found that optimizing the wing to obtain a 15% higher flutter speed only makes the structure 1.8% heavier.

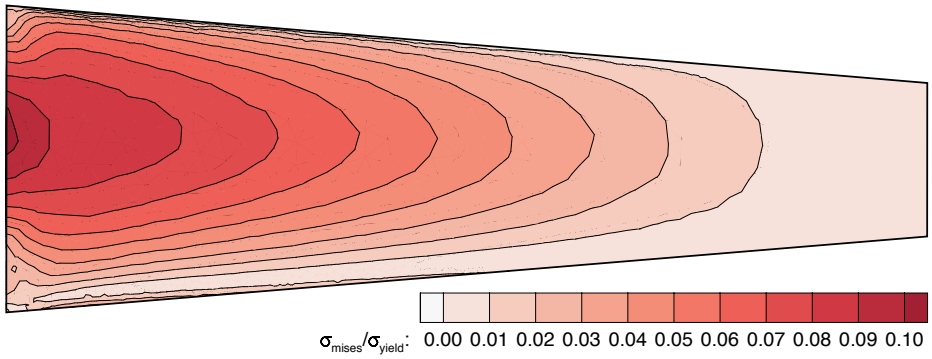

Fig. 10 Von Mises stress throughout design space for wing in transonic flow.

We consider an early-stage design study of a wing—with geometric parameters as listed in Table 3. It should be noted that this is not a real-world detailed design study, and merely an academic example of the developed methodology. These results are not intended to be used to deduce the relative benefit of aeroelastically-tailored lattice structures over other tailoring approaches. The structure is sized for a load case with dynamic pressure $q_\infty = 6535\ Pa$, wing lift coefficient $C_L = 0.8$, and Mach number $M_\infty = 0.75$. We also check flutter under these conditions. The material used in the wing is a polymer material with $E = 3.5\ GPa$, $\sigma_T = 50\ MPa$, $\sigma_C = 60\ MPa$, and $\rho = 1240\ kg/m^3$. In this study we assume all the load is taken up by the internals of the structure, neglecting any wing skin. The study can be extended to include a loaded wing skin, as mentioned in Ref. [34]. Note that we consider only the wing in this study, and consider the wing root to be fully clamped. The inclusion of this method in an overall aircraft design study could be a topic of future work, which this method should be fast enough for.

For the load case considered, the Von Mises stress through the solid internal domain of the wing is shown in Fig. 10, as computed using a structural FEM solver discussed in Appendix B of Ref. [35]. The aerodynamic loads are computed

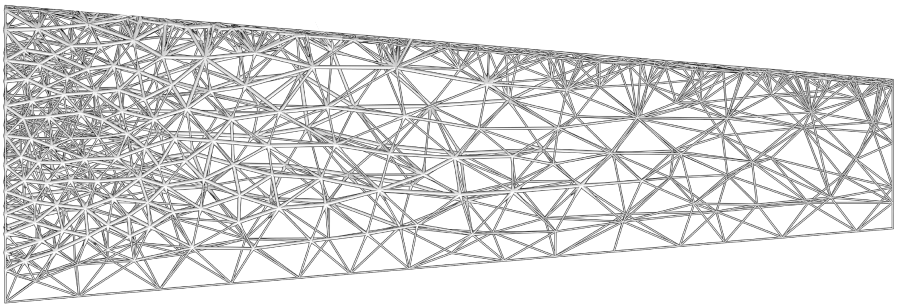

(a) Top view

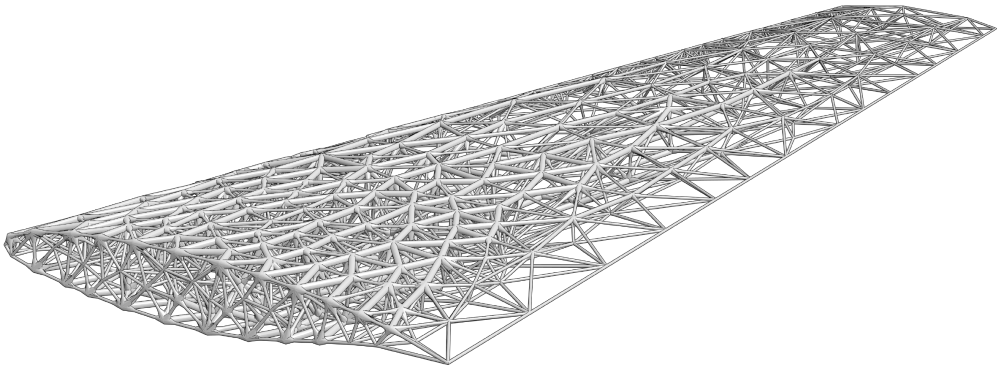

(b) 3D view, looking at root section

Fig. 11 Original lattice that is optimized without considering aeroelastic instabilities.

Table 3 Geometric parameters of wing

Parameter	Value
Root chord, c_r	1.0 m
Aspect ratio, $\mathcal{AR}$	6
Taper ratio, λ	0.5
Sweep, Λ	0°
Airfoil	C130 (from Ref. [45])

using a lifting-line method, in line with the aerodynamic model considered in Section II.B. The root is clearly highly loaded—especially near the center of the wing—whereas the tips are lightly loaded. The stress tensor for this load case is then used to generate a metric field, which in turn is used to generate the lattice topology. The struts of that lattice are subsequently optimized for minimum weight of the wing, subject to stress constraints—note that we will consider flutter constraints later in this section. The original optimized lattice—without considering flutter—is shown in Fig. 11. In this lattice the largest strut radius is allowed to be 2.5× larger than the smallest strut radius. This lattice has 629 nodes and 2,870 struts. The size of the full-order structural dynamic system is therefore (3540×3540). In this case, our lower-order model leads to approximately an order of magnitude lower computational cost. We should note that this is still a relatively small problem, and the low-order model's cost stays approximately constant with the size of the full-order model, leading to further cost savings for larger problems.

The flutter boundary for the original lattice is shown in Fig. 12. The model clearly exhibits typical transonic dip behavior, where the flutter speed is lowest for transonic Mach numbers and higher for subsonic and high transonic Mach numbers [46].

Problematically, this flutter speed V_f in Fig. 12 is too low and the wing starts fluttering at the design case considered. We therefore optimize the lattice again, but now add a flutter constraint that ensures the wing's flutter speed is at

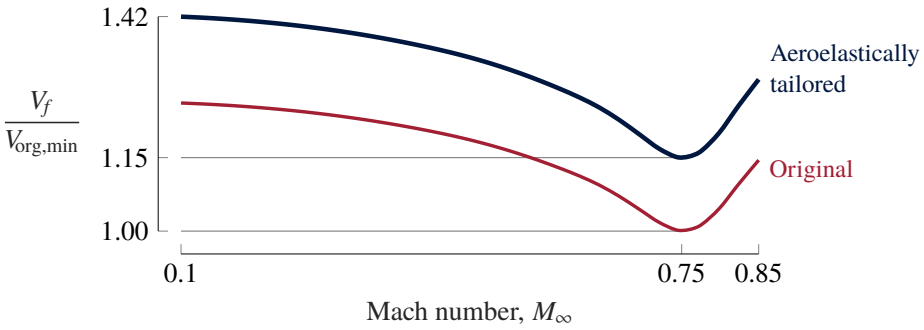

Fig. 12 Flutter boundary for both the original lattice and the aeroelastically-tailored lattice.

least 15% higher than the original lattice. To investigate the influence of initial condition on the optimization result, we consider three different initial conditions (Fig. 13): starting from the baseline design (optimized without flutter constraint), 25% larger cross-sectional areas than baseline design, and maximum cross-sectional area for all struts. Starting from the baseline design yields the lowest overall weight, which is to be expected given that the optimizer then already satisfies all constraints except the flutter constraint, and the main focus is then to satisfy the flutter constraint. Starting further away from the baseline design, the optimizer has to worry more about also satisfying stress-strain constraints, for instance, and can get stuck in a local minimum along the way due to the highly non-convex flutter constraint. In the rest of this section, we use the result with the baseline design as the initial condition.

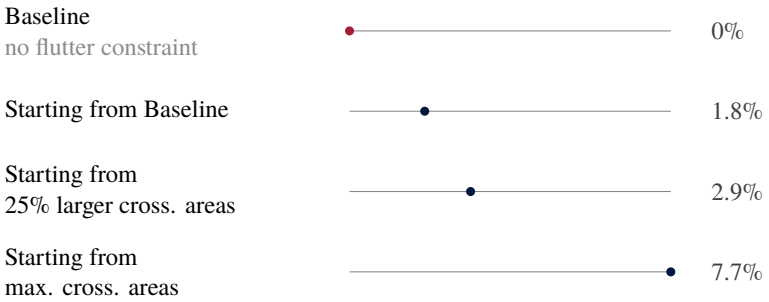

Fig. 13 Increase in wing mass compared to baseline for several aeroelastically tailored wings that are optimized using different initial conditions.

The resulting aeroelastically-tailored lattice is only 1.8% heavier than the original lattice. The flutter boundaries for both the original and the aeroelastically-tailored structure are shown in Fig. 12, which shows that the entire flutter boundary moves up for the aeroelastically-tailored lattice. Fig. 14 shows the final optimized lattice, where its struts are colored according to whether their cross-sectional area increased or decreased compared to the original lattice. We see that especially in the outboard region of the wing and near the trailing edge, the cross-sectional areas are increased. This is confirmed by the change of mass distribution and CG distribution along the span (Fig. 15), where we see that especially around 75% span the optimized lattice is heavier and the CG is shifted backwards. This also increases the stiffness of the outboard section of the wing, as that part of the wing is most flexible considering it has fewer struts, which are also fairly thin (Fig. 11). The change in stiffness of the internal structure of the wing, can be clearly deduced from the structural frequencies of the eigenmodes (Fig. 16), which are all at least 2.4% higher for the aeroelastically-tailored lattice (Table 4). We also validate these numbers against the full-order structural model in Table 4, which confirms the relative increase in structural frequency. All these changes are quite subtle, but remember that the overall mass increase is only 1.8%, so it is not expected that for instance the mass distribution changes drastically. However, these changes in local stiffness, CG position, and sectional mass are enough to increase the flutter speed by 15%.

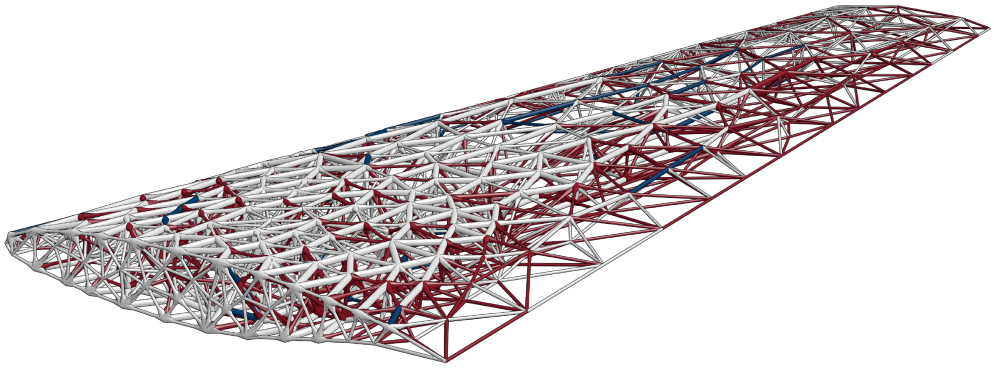

Fig. 14 Aeroelastically-tailored lattice. The cross-sectional area of each red struts is more than 2.5% larger than the cross-sectional area of the corresponding strut in the original lattice, whereas the cross-sectional area of each blue strut is smaller than the corresponding original strut by 1% or more.

Table 4 Comparison between relative increases in structural frequencies of wing from aeroelastically tailored wing to baseline wing.

Mode	Change in structural frequency (LOM)		Difference between LOM and FOM	
	LOM	FOM	Baseline	Aeroelastically-tailored
Mode I	+3.3%	+2.9%	+2.8%	+2.4%
Mode II	+3.4%	+3.3%	−3.1%	−3.2%
Mode III	+2.4%	+2.1%	+3.6%	+3.3%

V. Conclusion

This paper presented a design methodology for using lattice structures for the internal structure of a wing and tailoring the area of each member of the lattice for minimum weight and mitigating aeroelastic instabilities. The lattice structures are designed to align with the stress direction in the structure to result in an efficient structure. To keep the cost of evaluating the aeroelastic stability of the wing manageable, a low-order structural model is developed for the lattice structure. This low-order model is coupled to the physics-based low-order aerodynamic model to evaluate the aeroelastic eigenvalues of the system. The low-order model is computed using mappings between the deflections of the full-order lattice model and the equivalent beam model, and mappings between the forces on each node of the lattice to the moments and forces on the beam model. The structural frequencies of the low-order beam model have been compared against the structural frequencies of the full-order lattice model, where a maximum error of only 4% was observed for higher modes. This flutter model is then used to predict the flutter of the lattice structure and is included in the optimization problem to find the optimal cross-sectional area of each of the members of the lattice, while avoiding aeroelastic instabilities.

This approach to aeroelastic tailoring is applied to the design of the internal structure of a wing in transonic flow. It was found that including a flutter constraint in the optimization increases the flutter speed by 15%, while the weight of the structure is increased by only 1.8%, compared to the design where flutter was not constrained.

Funding Sources

This work was supported in part by the NASA LEARN program grant number NNX14AC73A and the SUTD-MIT International Design Center.

References

[1] Maute, K., Nikbay, M., and Farhat, C., "Sensitivity Analysis and Design Optimization of Three-Dimensional Non-Linear Aeroelastic Systems by the Adjoint Method," *International Journal for Numerical Methods in Engineering*, Vol. 56, No. 6,

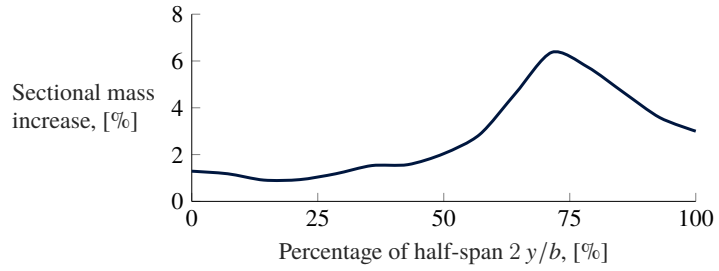

(a) Change in sectional mass distribution

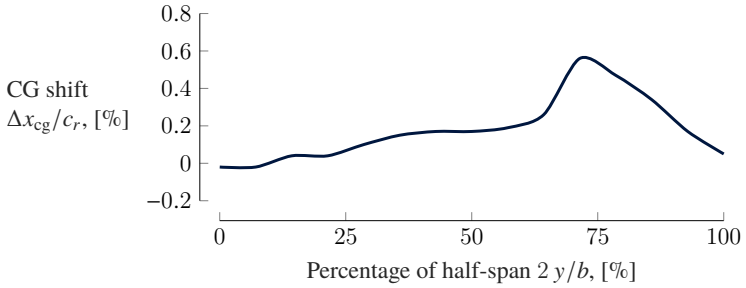

(b) Change in (sectional) CG distribution (as percentage of root chord), defined positive towards the trailing edge

Fig. 15 Changes in mass distribution and center of gravity position of the aeroelastically tailored lattice compared to the original lattice.

2003, pp. 911–933. doi:10.1002/nme.599.

[2] Martins, J. R. R. A., Alonso, J. J., and Reuther, J. J., "High-Fidelity Aerostructural Design Optimization of a Supersonic Business Jet," *Journal of Aircraft*, Vol. 41, No. 3, 2004, pp. 523–530. doi:10.2514/1.11478.

[3] Blair, M., Canfield, R. A., and Roberts, R. W., "Joined-Wing Aeroelastic Design with Geometric Nonlinearity," *Journal of Aircraft*, Vol. 42, No. 4, 2005, pp. 832–848. doi:10.2514/1.2199.

[4] Piperni, P., Abdo, M., Kafyeke, F., and Isikveren, A. T., "Preliminary Aerostructural Optimization of a Large Business Jet," *Journal of Aircraft*, Vol. 44, No. 5, 2007, pp. 1422–1438. doi:10.2514/1.26989.

[5] Kenway, G. K. W., and Martins, J. R. R. A., "Multipoint High-Fidelity Aerostructural Optimization of a Transport Aircraft Configuration," *Journal of Aircraft*, Vol. 51, No. 1, 2014, pp. 144–160. doi:10.2514/1.c032150.

[6] Balabanov, V., and Haftka, R. T., "Topology Optimization of Transport Wing Internal Structure," *Journal of Aircraft*, Vol. 33, No. 1, 1996, pp. 232–233.

[7] Locatelli, D., Mulani, S. B., and Kapania, R. K., "Wing-Box Weight Optimization using Curvilinear Spars and Ribs (SpaRibs)," *Journal of Aircraft*, Vol. 48, No. 5, 2011, pp. 1671–1684. doi:10.2514/1.c031336.

[8] Bendsøe, M. P., and Kikuchi, N., "Generating Optimal Topologies in Structural Design using a Homogenization Method," *Computer Methods in Applied Mechanics and Engineering*, Vol. 71, No. 2, 1988, pp. 197–224. doi:10.1016/0045-7825(88)90086-2.

[9] Bendsøe, M. P., and Sigmund, O., *Topology Optimization: Theory, Methods, and Applications*, Springer Science & Business Media, 2013.

[10] Gaynor, A. T., and Guest, J. K., "Topology Optimization Considering Overhang Constraints: Eliminating Sacrificial Support Material in Additive Manufacturing Through Design," *Structural and Multidisciplinary Optimization*, Vol. 54, No. 5, 2016, pp. 1157–1172. doi:10.1007/s00158-016-1551-x.

[11] Sethian, J. A., and Wiegmann, A., "Structural Boundary Design via Level-Set and Immersed Interface Methods," *Journal of Computational Physics*, Vol. 163, No. 2, 2000, pp. 489–528. doi:10.1006/jcph.2000.6581.

[12] Osher, S. J., and Santosa, F., "Level Set Methods for Optimization Problems Involving Geometry and Constraints: I. Frequencies of a Two-Density Inhomogeneous Drum," *Journal of Computational Physics*, Vol. 171, No. 1, 2001, pp. 272–288. doi:10.1006/jcph.2001.6789.

[13] Maute, K., and Reich, G., "An Aeroelastic Topology Optimization Approach for Adaptive Wing Design," *45th AIAA/ASME/ASCE/AHS/ASC Structures, Structural Dynamics & Materials Conference*, Palm Springs, California, 2004. doi:10.2514/6.2004-1805.

[14] Dunning, P. D., Stanford, B. K., and Kim, H. A., "Coupled Aerostructural Topology Optimization Using a Level Set Method for 3D Aircraft Wings," *Structural and Multidisciplinary Optimization*, Vol. 51, No. 5, 2014, pp. 1113–1132. doi:10.1007/s00158-014-1200-1.

[15] Kambampati, S., Townsend, S., and Kim, H. A., "Aeroelastic Level Set Topology Optimization for a 3D Wing," *2018 AIAA/ASCE/AHS/ASC Structures, Structural Dynamics, and Materials Conference*, Kissimmee, Florida, 2018. doi:10.2514/6.2018-2151.

[16] Stanford, B. K., and Dunning, P. D., "Optimal Topology of Aircraft Rib and Spar Structures Under Aeroelastic Loads," *Journal of Aircraft*, Vol. 52, No. 4, 2015, pp. 1298–1311. doi:10.2514/1.c032913.

[17] Townsend, S., Picelli, R., Stanford, B., and Kim, H. A., "Structural Optimization of Platelike Aircraft Wings Under Flutter and Divergence Constraints," *AIAA Journal*, Vol. 56, No. 8, 2018, pp. 3307–3319. doi:10.2514/1.j056748.

[18] Aage, N., Andreassen, E., Lazarov, B. S., and Sigmund, O., "Giga-Voxel Computational Morphogenesis for Structural Design," *Nature*, Vol. 550, No. 7674, 2017, p. 84. doi:10.1038/nature23911.

[19] Haddadpour, H., and Zamani, Z., "Curvilinear Fiber Optimization Tools for Aeroelastic Design of Composite Wings," *Journal of Fluids and Structures*, Vol. 33, 2012, pp. 180–190. doi:10.1016/j.jfluidstructs.2012.05.008.

[20] Stodieck, O., Cooper, J. E., Weaver, P. M., and Kealy, P., "Improved Aeroelastic Tailoring using Tow-Steered Composites," *Composite Structures*, Vol. 106, 2013, pp. 703–715. doi:10.1016/j.compstruct.2013.07.023.

[21] Guo, S., Cheng, W., and Cui, D., "Aeroelastic Tailoring of Composite Wing Structures by Laminate Layup Optimization," *AIAA Journal*, Vol. 44, No. 12, 2006, pp. 3146–3150. doi:10.2514/1.20166.

[22] Dillinger, J., Klimmek, T., Abdalla, M. M., and Gürdal, Z., "Stiffness Optimization of Composite Wings with Aeroelastic Constraints," *Journal of Aircraft*, Vol. 50, No. 4, 2013, pp. 1159–1168. doi:10.2514/1.c032084.

[23] Stanford, B. K., Jutte, C. V., and Wieseman, C. D., "Trim and Structural Optimization of Subsonic Transport Wings using Nonconventional Aeroelastic Tailoring," *AIAA Journal*, Vol. 54, No. 1, 2016, pp. 293–309. doi:10.2514/6.2014-2596.

[24] Walker, D., Liu, D., and Jennings, A. L., "Wing Design Utilizing Topology Optimization and Additive Manufacturing," *57th AIAA/ASCE/AHS/ASC Structures, Structural Dynamics, and Materials Conference*, San Diego, California, 2016. doi:10.2514/6.2016-1246.

[25] Rehme, O., "Cellular Design for Laser Freeform Fabrication," Ph.D. thesis, Technical University Hamburg, Göttingen, 2010.

[26] Vigliotti, A., and Pasini, D., "Analysis and Design of Lattice Materials for Large Chord and Curvature Variations in Skin Panels of Morphing Wings," *Smart Materials and Structures*, Vol. 24, No. 3, 2015, p. 037006. doi:10.1088/0964-1726/24/3/037006.

[27] Jenett, B., Calisch, S., Cellucci, D., Cramer, N., Gershenfeld, N., Swei, S., and Cheung, K. C., "Digital Morphing Wing: Active Wing Shaping Concept Using Composite Lattice-Based Cellular Structures," *Soft Robotics*, Vol. 4, No. 1, 2017, pp. 33–48. doi:10.1089/soro.2016.0032.

[28] Ganguli, R., and Chopra, I., "Aeroelastic Tailoring of Composite Couplings and Blade Geometry of a Helicopter Rotor using Optimization Methods," *Journal of the American Helicopter Society*, Vol. 42, No. 3, 1997, pp. 218–228. doi:10.4050/jahs.42.218.

[29] Glaz, B., Friedmann, P. P., and Liu, L., "Surrogate-Based Optimization of Helicopter Rotor Blades for Vibration Reduction in Forward Flight," *Structural and Multidisciplinary Optimization*, Vol. 35, No. 4, 2008, pp. 341–363. doi:10.1007/s00158-007-0137-z.

[30] Pagano, A., Federico, L., Barbarino, M., Guida, F., and Aversano, M., "Multi-Objective Aeroacoustic Optimization of an Aircraft Propeller," *12th AIAA/ISSMO Multidisciplinary Analysis and Optimization Conference*, Victoria, British Columbia, Canada, 2008. doi:10.2514/6.2008-6059.

[31] Opgenoord, M. M. J., Drela, M., and Willcox, K. E., "Physics-Based Low-Order Model for Transonic Flutter Prediction," *AIAA Journal*, Vol. 56, No. 4, 2018, pp. 1519–1531. doi:10.2514/1.J056710.

[32] Opgenoord, M. M. J., Drela, M., and Willcox, K. E., "Influence of Transonic Flutter on the Conceptual Design of Next-Generation Transport Aircraft," *AIAA Journal*, Vol. 57, No. 5, 2019, pp. 1973–1987. doi:10.2514/1.j057302.

[33] Palacios, F., Colonno, M. R., Aranake, A. C., Campos, A., Copeland, S. R., Economon, T. D., Lonkar, A. K., Lukaczyk, T. W., Taylor, T. W., and Alonso, J. J., "Stanford University Unstructured (SU2): An Open-Source Integrated Computational Environment for Multi-Physics Simulation and Design," *51st AIAA Aerospace Sciences Meeting*, Grapevine, Texas, 2013. doi:10.2514/6.2013-287.

[34] Opgenoord, M. M. J., and Willcox, K. E., "Design for Additive Manufacturing: Cellular Structures in Early-Stage Aerospace Design," *Structural and Multidisciplinary Optimization*, 2019. Accepted on April 30, 2019.

[35] Opgenoord, M. M. J., "Transonic Flutter Prediction and Aeroelastic Tailoring for Next-Generation Transport Aircraft," Ph.D. thesis, Department of Aeronautics & Astronautics, Massachusetts Institute of Technology, 9 2018.

[36] Yano, M., and Darmofal, D. L., "An Optimization-Based Framework for Anisotropic Simplex Mesh Adaptation," *Journal of Computational Physics*, Vol. 231, No. 22, 2012, pp. 7626–7649. doi:10.1016/j.jcp.2012.06.040.

[37] Zienkiewicz, O. C., *Finite element method : its basis and fundamentals*, Butterworth-Heinemann, Amsterdam Boston, 2013.

[38] Ohsaki, M., *Optimization of Finite Dimensional Structures*, CRC Press/Taylor & Francis, Boca Raton, 2011.

[39] Ringertz, U. T., "On Structural Optimization with Aeroelasticity Constraints," *Structural Optimization*, Vol. 8, No. 1, 1994, pp. 16–23. doi:10.1007/bf01742928.

[40] Wächter, A., and Biegler, L. T., "On the Implementation of an Interior-Point Filter Line-Search Algorithm for Large-Scale Nonlinear Programming," *Mathematical Programming*, Vol. 106, No. 1, 2006, pp. 25–57. doi:10.1007/s10107-004-0559-y.

[41] Giles, M. B., "Collected Matrix Derivative Results for Forward and Reverse Mode Algorithmic Differentiation," *Advances in Automatic Differentiation*, Springer Berlin Heidelberg, 2008, pp. 35–44. doi:10.1007/978-3-540-68942-3_4.

[42] Giles, M., "An Extended Collection of Matrix Derivative Results for Forward and Reverse Mode Automatic Differentiation," Tech. Rep. 08/01, Computing Laboratory, Oxford University, Oxford, United Kingdom, 2008.

[43] Griewank, A., "On Automatic Differentiation," *Mathematical Programming - Recent Developments and Applications*, Kluwer Academic Publishers, Amsterdam, 1989, pp. 83–108.

[44] BAMPTON, M. C. C., and R. R. CRAIG, J., "Coupling of substructures for dynamic analyses." *AIAA Journal*, Vol. 6, No. 7, 1968, pp. 1313–1319. doi:10.2514/3.4741.

[45] Drela, M., "N3 Aircraft Concept Designs and Trade Studies – Appendix," Tech. Rep. NASA CR-2010-216794/VOL2, 2010.

[46] Bendiksen, O. O., "Review of Unsteady Transonic Aerodynamics: Theory and Applications," *Progress in Aerospace Sciences*, Vol. 47, No. 2, 2011, pp. 135–167. doi:10.1016/j.paerosci.2010.07.001.

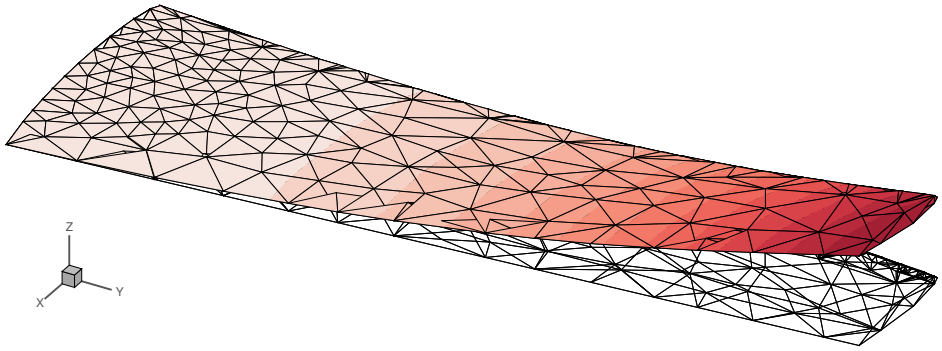

(a) 1st mode (bending), frequency 3.3% higher for tailored lattice

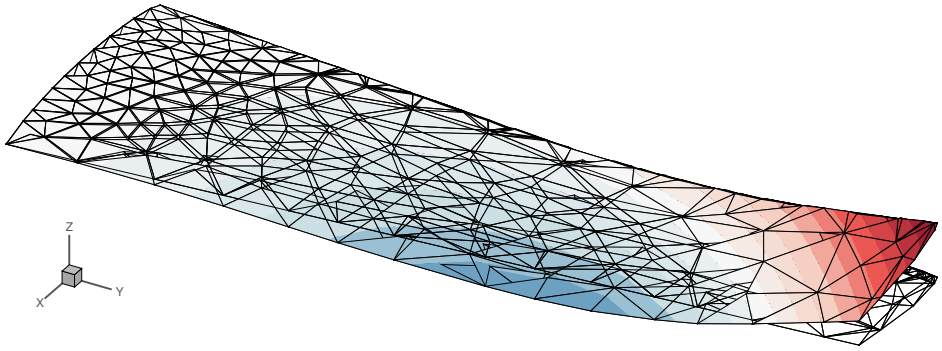

(b) 2nd mode (coupled bending-torsion), frequency 3.4% higher for tailored lattice

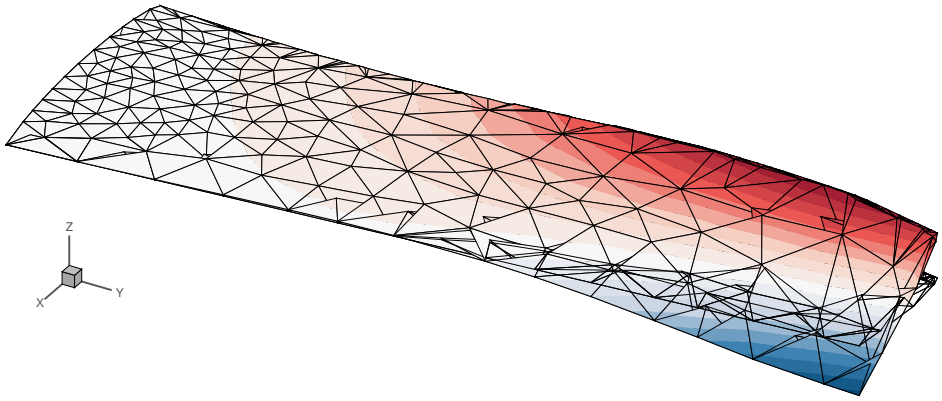

(c) 3rd mode (torsion), frequency 2.4% higher for tailored lattice

Fig. 16 Eigenmodes for optimized wing lattice. These are essentially identical to the eigenmodes of the original wing lattice.